




A-site double-lanthanide-doped $\text{La}_{1-x}\text{Pr}_x\text{BaCo}_2\text{O}_{5+\delta}$ cathode materials for intermediate-temperature solid oxide fuel cells

Dacheng Zhou¹, Chuan Yuan¹, Xiyong Chen^{1,*} , Fangze Chen¹, Xueqing Xiong¹, Yihui Liu^{2,*}, Jialin Yan¹, and Toyohisa Fujita¹

¹Guangxi Key Laboratory of Processing for Non-Ferrous Metals and Featured Materials, School of Resources, Environment and Materials, Guangxi University, Nanning 530004, Guangxi, China

²Hubei Key Laboratory of Advanced Technology for Automotive Components and Hubei Collaborative Innovation Center for Automotive Components Technology, Wuhan University of Technology, Wuhan 430070, Hubei, China

Received: 6 March 2022

Accepted: 24 June 2022

Published online:

27 July 2022

© The Author(s), under exclusive licence to Springer Science+Business Media, LLC, part of Springer Nature 2022

ABSTRACT

Double-perovskite materials $\text{La}_{1-x}\text{Pr}_x\text{BaCo}_2\text{O}_{5+\delta}$ (LPBCO), suitable for the application of intermediate-temperature solid oxide fuel cell (IT-SOFC) and other electrochemical devices, were successfully prepared through solid-state reaction method. The effects of La and Pr doping ratios on the crystallographic structure, thermochemical stability, thermal expansion, electrical conductivity, and electrochemical polarizations were analyzed and discussed. The X-ray diffraction results show that the crystal structure changes from single perovskite to double perovskite with the increase in Pr doping content. LPBCOs present excellent chemical stability with conventional electrolyte GDC at less than 1100 °C. The thermal expansion can be effectively reduced upon doping of Pr. The materials demonstrate high electrical conductivity even under relatively low temperatures, i.e., LP-73 ($x = 0.3$ with single perovskite) has the highest conductivity at 1680 S/cm at 400 °C. Among the double-perovskite compositions, LP-55 presents the highest performance in electrical conductivity though. Analysis of the electrochemical impedance spectra of LPBCOs symmetric cells reveals low area specific polarization resistances for these double-lanthanide-doped double-perovskite materials, and the charge transfer is determined as the dominating sub-process for the oxygen transport through the materials. All the findings show that $\text{La}_{1-x}\text{Pr}_x\text{BaCo}_2\text{O}_{5+\delta}$ possesses excellent oxygen reduction activity and is promising for the application in IT-SOFCs.

Handling Editor: Till Froemling.

Address correspondence to E-mail: xiyongchen@gxu.edu.cn; liuyihui@whut.edu.cn

Introduction

Solid oxide fuel cell (SOFC) is a kind of clean energy technology that can directly convert the chemical energy of fuel into electric energy [1–4]. Early solid oxide fuel cells used yttrium-stabilized zirconia (YSZ) as the solid electrolyte, which typically requires high operating temperatures to guarantee the acceptable ionic conductivity in SOFC applications. Nevertheless, high operating temperature (above 800 °C) brings great challenges to all parts of the fuel cell to construct a cost-effective, stable, and durable system [5]. Intermediate-temperature (500–800 °C) solid oxide fuel cells (IT-SOFC) utilizing low-to-medium temperature solid electrolytes (for example, $\text{Ce}_{0.8}\text{Gd}_{0.2}\text{O}_{2-\delta}$ (GDC) [6], $\text{La}_{0.8}\text{Sr}_{0.2}\text{Ga}_{0.85}\text{Mg}_{0.15}\text{O}_{2.825}$ (LSMG) [7], $\text{BaZr}_{0.1}\text{Ce}_{0.7}\text{Y}_{0.3}\text{O}_{3-d}$ (BZCY) [8] therefore became one of the most attracting directions in this field [9–11]. However, with the reducing working temperatures, the electrical and electrochemical activities of the high-temperature SOFC cathode materials will be significantly hampered, which eventually leads to the lower SOFC performance. It is therefore extremely urgent to develop new and low-cost high-performance cathode materials with high conductivity, excellent electrochemical catalytic performance, and good thermal matching performance with the IT-SOFC electrolytes at low-to-medium temperatures [12].

To date, perovskite-type oxides are recognized as the most suitable SOFC cathode materials due to their advantages of high catalytic activity, low polarization resistance, good electrical conductivity, etc. [13–15]. The most frequently investigated perovskite-type oxides include $\text{La}_{1-x}\text{Sr}_x\text{CoO}_{3-\delta}$ (LSC) [16, 17], $\text{La}_{1-x}\text{Sr}_x\text{Co}_{0.2}\text{Fe}_{0.8}\text{O}_{3-\delta}$ (LSCF) [18], $\text{Ba}_{0.5}\text{Sr}_{0.5}\text{Co}_{0.2}\text{Fe}_{0.8}\text{O}_{3-\delta}$ (BSCF) [19], $\text{LnBaCo}_2\text{O}_{5+\delta}$ (LnBCO, Ln = lanthanide element) [20]. Among these perovskite materials, LnBCOs with double-perovskite structures have recently been considered as promising IT-SOFC cathode materials due to the attractive electrochemical performance [20, 21].

Double-perovskite LnBCO materials typically have an alternately layered LnO–CoO–BaO structure along the *c*-axis due to the relatively large ionic difference between the lanthanide ion and barium ion in the A sites [22]. Besides, the double-perovskite LnBaCO generally has high concentration of oxygen vacancies in the Ln–O layers which facilitate the surface and

bulk oxygen transfer as well as the oxygen exchange reaction on the surface [23]. In fact, a lot of studies have been carried out on the structure, magnetism, and oxygen ion transport properties of LnBCO oxides at moderate temperatures, which revealed that the electron and oxygen ion conductivity of this type of double-perovskite oxide are particularly outstanding [20, 21, 24]. Among them, LaBCO typically forms a cubic A-site cation disordered perovskites ($\text{La}_{0.5}\text{Ba}_{0.5}\text{CoO}_{3-\delta}$) because of the much close effective ionic radii of La^{3+} and Ba^{2+} . The double-perovskite LaBCO ($\text{LaBaCo}_2\text{O}_{5+\delta}$) can be obtained by controlling the calcination process in a highly oxygen-free atmosphere [25]. Both the single- and double-perovskite LaBCO exhibited high electrical and electrochemical performances [26]. Comparatively, the A-site ordered LaBCO demonstrated higher electrical conductivity and electrochemically catalytic activity. However, due to its metastable phase nature, the double-perovskite LaBCO is difficult to maintain its structure in the applications. People therefore studied a lot on other $\text{LnBaCo}_2\text{O}_{5+\delta}$ (Ln = Pr, Nd, Sm, Gd, Y) materials with stable double-perovskite structures and found that these materials also showed reasonable excellent performances [27]. Especially, PrBCO demonstrates the lowest cathodic polarization resistance and a higher conductivity than the other LnBCOs, which to some extent illustrates that PrBCO would be a more suitable cathode material for the potential application of SOFCs [22, 28, 29]. To further enhance the overall performance of PrBCO, strategies on partial doping of A-site Ba with alkaline elements such as Sr and Ca have been adopted [30, 31]. The investigations revealed that the Sr- or Ca-substitution can improve the electrical conductivity and the electrochemical activity. But unfortunately it also found that SrO and BaO will segregate at high temperatures (over 800 °C), resulting in a gradual deterioration of the catalytic effect [32]. The influence of partial replacement of A-site ions with La^{3+} had also been evaluated, and the results indicated the substitution of Lanthanum on both A-site Gd^{3+} and Ba^{2+} reduces the oxygen vacancies in the materials but enhances the electrical conductivity and the area specific polarization resistance [33]. This may imply that double-lanthanide doping on the A-site lanthanide position may be another promising strategy to enhance the overall properties of the double-perovskite LnBCO materials.

This work is to prepare a series of $\text{La}_{1-x}\text{Pr}_x\text{BaCo}_2\text{O}_{5+\delta}$ (LPBCO) with various La/Pr ratios, and to evaluate the influence of the lanthanide ratio on the corresponding phase structures, thermochemical compatibility, thermal expansion, electrical conductivity, and polarization impedance of the materials. Through the investigation, it is expected to provide an insight on developing LnBCO double-perovskite cathode materials with A-site double-lanthanide-doping strategy to obtain excellent comprehensive performance at low and medium temperatures.

Experimental

Sample preparation

Powder synthesis

$\text{La}_{1-x}\text{Pr}_x\text{BaCo}_2\text{O}_{5+\delta}$ ($x = 0, 0.1, 0.3, 0.5, 0.7, 0.9, 1.0$) powders doped with double lanthanides were synthesized by the traditional solid-state reaction method [22, 34]. For the sake of convenience, $\text{La}_{1-x}\text{Pr}_x\text{BaCo}_2\text{O}_{5+\delta}$ with $x = 0$ to 1.0 are thereafter denoted as LaBCO, LP-91, LP-73, LP-55, LP-37, LP-19, and PrBCO, respectively, in this paper. Prior to the synthesis, the starting materials of La_2O_3 , Pr_6O_{11} , Co_3O_4 , BaCO_3 were preheated at 950 °C (for Lanthanide material) and 120 °C (for other chemicals), for 12 h to remove the physically and/or chemically adsorbed water and CO_2 or restore its original oxide form from its chemically transformed matters during storage and transportation. All these chemicals were purchased from Aladdin Chemicals, China with the purity of 99.9%. The pretreated raw materials were then weighed in exact stoichiometric ratios and ball-ground in acetone at 300 rpm for 12 h. After grounding, the powder mixtures were calcined at 1100 °C for another 12 h in air to obtain the desired materials. $\text{Ce}_{0.8}\text{Gd}_{0.2}\text{O}_{1.9}$ (GDC) electrolyte powder was purchased from Ningbo SOFCMAN Energy Technology Co, LTD (China) without further treatment.

Dense bar-shaped samples preparation

Bar-shaped samples were prepared for the evaluation of electrical conductivity and thermal expansion. The as-calcined powder was sufficiently ground by adding 5% PVA as adhesives. Green bars with

dimensions of 30 mm × 3 mm × 3 mm were obtained by uniaxially pressing the well-ground powders at 200 MPa followed by cold isostatic pressing at 300 MPa and sintering at 1150 °C for 3 h in air. The relative densities of the sintered samples were about 96% tested by an Archimedes water displacement method. For the samples for thermal expansion evaluation, both ends of the samples were polished. For the samples for electrical conductivity tests, the sample bars were ground into about 1 mm in thickness at first. Each sample was later wrapped with four independent silver wires in distinct distances. Silver paste was used to secure the silver wires for the conductivity test after annealing at 800 °C.

Symmetric cells fabrication

Symmetric cells of $\text{La}_{1-x}\text{Pr}_x\text{BaCo}_2\text{O}_{5+\delta}/\text{GDC}/\text{La}_{1-x}\text{Pr}_x\text{BaCo}_2\text{O}_{5+\delta}$ were used for the analysis of the cathodic polarization resistance. To facilitate the electrolyte sintering process and reduce the sintering temperature, 5wt% Fe_2O_3 sintering aid was mixed with as-purchased GDC powder [35]. Dense GDC electrolyte disks with a diameter of around 15 mm and relative density of over 95% were then obtained after sintering the pressed GDC green pellets at 1400 °C for 12 h in air. The electrolyte disks were thereafter polished and ultrasonically cleaned prior to the screen printing of the cathode slurry onto both sides of the GDC electrolyte. The cathode slurry was prepared by well mixing the cathode powder with certain amounts of ethyl cellulose (pore former) and terpineol (dispenser). When both sides of the GDC electrolyte disk were coated with the cathode slurry, the assembly was then sintered at 950 °C for 3 h. The microscopic observation reveals good contact of the porous cathode and the dense electrolyte (Fig. S1 in Supplementary Information). Silver meshes, as current collectors, were attached onto the porous electrodes with the assistance of silver paste and annealing at 800 °C for 10 min.

Materials characterization

Thermal expansion analysis

Thermal expansion behaviors of LPBCO samples were measured from 30 to 900 °C using a dilatometer (Netzsch, DIL402C) at a heating rate of 5 K min⁻¹

under atmospheres with different oxygen activities ($pO_2 = 0.21, 0.01, \text{ and } 10^{-4} \text{ atm}$). A continuous gas flow at a flow rate of $60 \text{ ml}\cdot\text{min}^{-1}$ was sent into the chamber to keep the sample at a fixed gas environment.

Electrical conductivity measurements

The electrical conductivity measurements were carried out using an electrochemical workstation (Chenhua, CHI760E) with a 4-probe DC configuration in a temperature range of $400\text{--}800 \text{ }^\circ\text{C}$ and under a specific atmosphere with $pO_2 = 0.21, 0.01, \text{ and } 10^{-4} \text{ atm}$, respectively.

Electrochemical performance evaluation

Electrochemical impedance spectrum (EIS) of the symmetrical cell LPBCO/GDC/LPBCO under certain temperature and pO_2 environment was used to analyze the cathodic polarization resistance. The EIS was obtained using an electrochemical workstation (Solartron, 1260A + 1287A) with AC amplitude of 10 mV around open circuit voltage and a test frequency range of $10^{-2}\text{--}10^5 \text{ Hz}$. The sample temperature was controlled in the range of $600\text{--}750 \text{ }^\circ\text{C}$ and the gas atmosphere surrounding the sample was controlled at $pO_2 = 0.21, 0.01, \text{ and } 10^{-4} \text{ atm}$.

Phase and morphological characterization

The phase structures of LPBCO samples under this study were analyzed by an X-ray powder diffractometer (MINIFLEX600, Rigaku) using $\text{Cu K}\alpha$ radiation ($\lambda = 1.5406 \text{ \AA}$) with the diffraction angle between 20° and 80° , a continuous scanning speed at $10^\circ/\text{min}$, an accelerating voltage at 40 kV and a current at 100 mA . The corresponding space group and crystal cell parameters were refined with the Rietveld method using the Fullprof program [36]. A scanning electron microscopy (Hitachi S3400N) was used to characterize the surface and cross section morphologies of the symmetrical cells.

Results and discussion

Phase structure and thermochemical stability

Figure 1 shows the room temperature XRD patterns of the as-calcined $\text{La}_{1-x}\text{Pr}_x\text{BaCo}_2\text{O}_{5+\delta}$ ($0 \leq x \leq 1.0$) samples. The XRD pattern of PrBCO ($x = 1.0$) demonstrates a typical diffraction of a double-perovskite structure with ordered Pr–O layer and Ba–O layer in an alternative sequence along the c -axis [29, 34]. But for LaBCO ($x = 0.0$), it appears a single-perovskite phase with La and Ba randomly distributed in A sites because of the relatively closer effective ionic radii of La^{3+} [37] (1.36 nm at coordination number/CN of 12 vs. 1.27 nm for Pr^{3+} [37]) and Ba^{2+} (1.61 nm , CN = 12 [37]), which is consistent with the literature findings [38, 39].

Further Rietveld refinement of these two components reveals the space groups of $\text{Pm}\bar{3}\text{m}$ (cubic) and $\text{P4}/\text{mmm}$ (tetragonal) can be ascribed to LaBCO and PrBCO, respectively. Figure 2 shows the corresponding Rietveld refinement results of LaBCO and PrBCO with good fittings. Because of the relatively smaller radius of Pr^{3+} , increasing Pr substitution of La will generally reduce the average effective ionic radius of A-site lanthanides in the composition, which further enlarges the ionic radius difference between the lanthanide ions and Ba^{2+} . Therefore, double-perovskite structure becomes the stable phase for those compositions with higher Pr doping levels. When take look at those diffraction peaks of the crystallographic planes parallel to the c -axis, such as

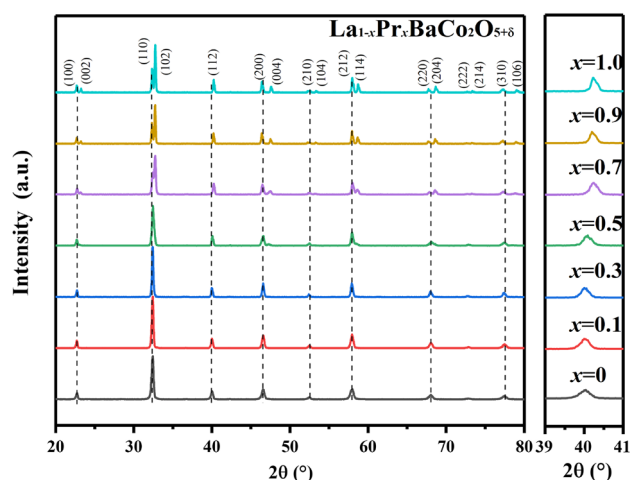


Figure 1 XRD patterns of as-calcined $\text{La}_{1-x}\text{Pr}_x\text{BaCo}_2\text{O}_{5+\delta}$ powders.

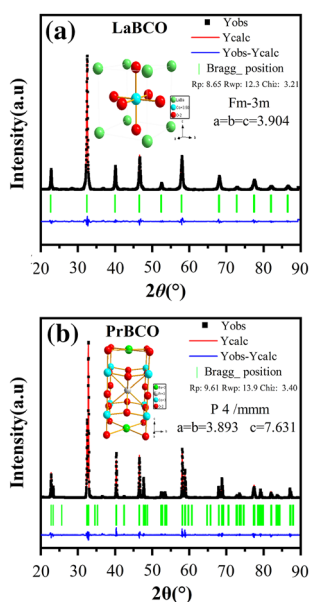


Figure 2 Refined XRD patterns of **a** LaBCO and **b** PrBCO.

(100), (200), (110), (210), and so on, the corresponding peaks have almost same diffraction angles no matter what La/Pr ratio is in the composition. This is because the cell parameters along the a - b plane are mainly controlled by the Ba–Ba distance on the Ba–O layer. Owing to the smaller effective ionic radii of lanthanide elements, atomic distance along the c -axis shrinks which results in the appearance of the satellite diffraction peaks, (002), (102), (004), etc., corresponding to those above-mentioned crystallographic planes. With the increase in Pr content in LPBCO, the gradually reduced average effective ionic radius of the lanthanides leads to a decreased c -axis cell parameter and therefore increased diffraction angles of (002), (102), (004), etc., as shown in Fig. 1. The non-splitting diffraction peak of (112) in double perovskites, which corresponds to (111) plane in single perovskite, to some extent indicates the pure phase for each composition with different La/Pr ratios in this study. Phase transition may occur at $0.3 < x < 0.5$ in which a single-perovskite and a double-perovskite phases coexist in the materials. However, due to the thermodynamic stability, the two stable phases are expected to have different La/Pr ratios in the compositions, i.e., a La-rich composition with a single-perovskite structure and a Pr-rich phase with double-perovskite structure. According to the XRD patterns, the (112) reflection of Pr-rich double perovskite typically has higher diffraction angle than the (111) reflection of La-rich single

perovskite. Peak splitting corresponding to the overlapping of the (112) and (111) reflections should be identified in the case of mixed phases. As presented previously, only a single diffraction peak can be observed in the XRD pattern for each composition, it is reasonable to assume pure phase for all the investigated compositions in this study. Since (004) diffraction starts to split from the (200) diffraction in LP-55 (Fig. 1), it is therefore concluded double-perovskite structures for LPBCOs with $x \geq 0.5$ and single perovskite for those with $x \leq 0.3$.

The thermochemical compatibility of suitable cathode materials with the electrolyte is one of the criteria for IT-SOFC applications. In this study, the thermochemical compatibility of LPBCO and GDC electrolyte were evaluated. Figure 3 shows the XRD patterns of LaBCO, LP-73, LP-37, and PrBCO powders mixed with GDC at a 1:1 mass ratio and fired at 1100 °C and 1150 °C for 12 h. None of the four samples reacted with electrolyte GDC at the calcination temperature of 1100 °C (Fig. 3a). However, when the firing temperature rises to 1150 °C, it can be seen from Fig. 3b that all the XRD patterns of LaBCO, LP-73, LP-37, and PrBCO with GDC have obvious impurity peaks. The results show that LaBCO, LP-73, LP-37, and PrBCO samples have excellent thermochemical compatibility with GDC electrolyte when the co-firing temperature is below 1100 °C.

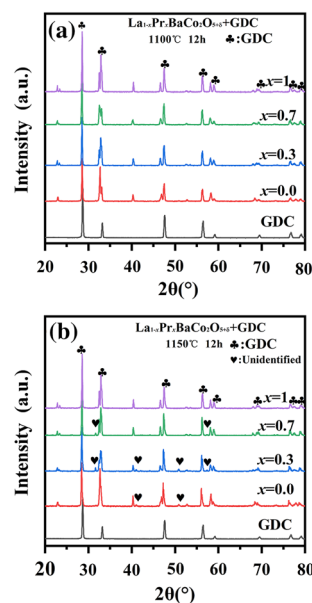
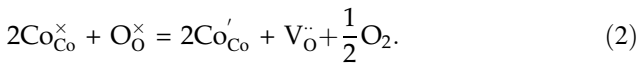
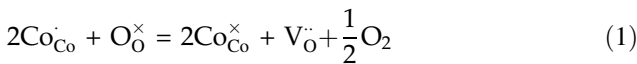


Figure 3 XRD patterns of $\text{La}_{1-x}\text{Pr}_x\text{BaCo}_2\text{O}_{5+\delta}$ and GDC mixture after firing at **a** 1100 °C and **b** 1150 °C for 12 h.

Thermal expansion behaviors

The thermal expansion curves for $\text{La}_{1-x}\text{Pr}_x\text{BaCo}_2\text{O}_{5+\delta}$ ($0 \leq x \leq 1$) in air is shown in Fig. 4a. At the low temperature range (below ~ 350 °C), all the samples expand roughly linearly with the temperature. However, as the temperature exceeds ~ 350 °C, extra expansion behavior can be identified for almost all the samples. This is particularly due to the formation of oxygen vacancies in the samples when the temperature is over 350 °C.

In order to maintain the electrical neutrality, part of the Co ions are reduced and more low-valence Co ions are formed. The XPS data shown in Fig. S2 reveals that starting composition of LP-55 at room temperature contains only Co^{4+} and Co^{3+} . However, when the temperature continues increasing, more oxygen vacancies are formed and the overall oxygen stoichiometry would be reduced down below 5.5 at higher temperatures around 800 °C in air (Fig. S3-b). Assuming unchangeable valence of Ln and Ba ions, the average Co valence would be less than 3, which means the production of Co^{2+} . Hence, the formation of oxygen vacancies along with the Co valence change can be represented according to the following defect equations in Kroger–Vink notation [40]:



As a result, the average effective ionic radius of cobalt ions becomes larger so that extra lattice expansion other than the pure thermal expansion (denoted as $\Delta\epsilon_T$) which is not related to the chemical state variations in the materials is introduced. Additionally, as the valence state of cobalt ion decreases, the outer electrons of cobalt ion may also experience a spin transition from low to high spin state [15], which will result in the ionic radius increase in Co ions as well. Since this extra expansion is related to the oxygen vacancy concentration or the valence state of Co ions in the materials, it can sometimes refer to the chemical expansion, symbolized as $\Delta\epsilon_C$ [41]. Overall thermal expansion coefficient (TEC) derived from the expansion curve between 500 and 900 °C is shown in Fig. 4b. It clearly shows the TEC increases with lowering the Pr doping level. It should be mentioned that the TEC presented in Fig. 4b is measured from the reflection temperature of each component in a

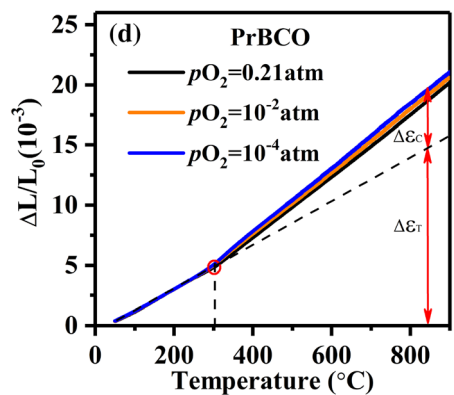
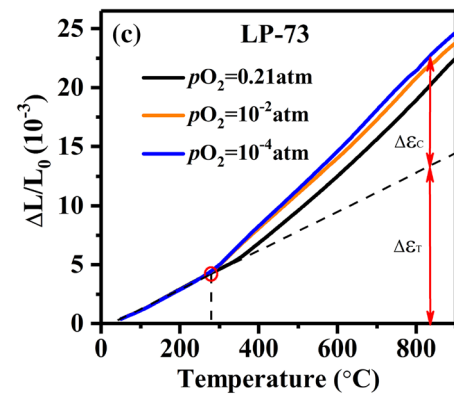
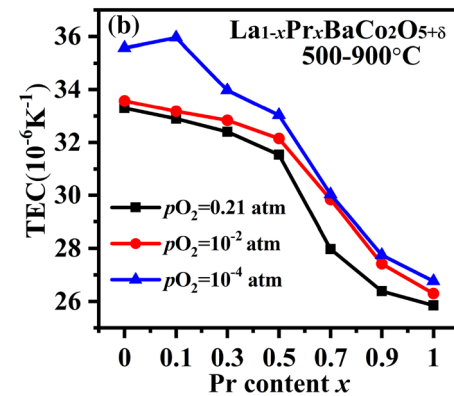
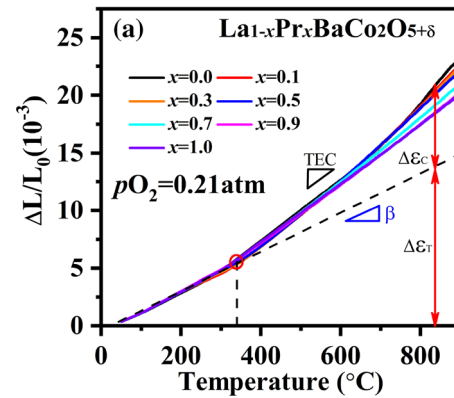


Figure 4 **a** Thermal expansion curves of $\text{La}_{1-x}\text{Pr}_x\text{BaCo}_2\text{O}_{5+\delta}$ samples in air; **b** the average overall thermal expansion coefficient (TEC) of $\text{La}_{1-x}\text{Pr}_x\text{BaCo}_2\text{O}_{5+\delta}$ at different oxygen partial pressures, measured from the inflection temperature at which chemical expansion starts; and thermal expansion curves of **c** LP-73 and **d** PrBCO in the atmospheres with different $p\text{O}_2$. The red circle in each figure indicates the inflection temperature, and the dash line extrapolated from the low-temperature expansion curve simulates the pure thermal expansion part of the total expansion in the higher temperature range.

particular gas environment. Since the chemical expansion contributes significantly to the overall expansion, the obtained TEC values indeed reflect the combined effects of both thermal and chemical expansions. Interestingly, more extra chemical expansion could be found for those materials with $0 \leq x \leq 0.5$ when the temperature is above roughly 700°C . However, the TGA analysis of the materials (Fig. S3) shows the oxygen loss is literally linear with temperature below 900°C . In other words, the oxygen vacancy in the materials varies linearly with temperature in the whole temperature range under investigation. Therefore, this additionally increased expansion in the high temperature range cannot be solely explained with the valence change of Co ions. Significantly increased spin transition of low-valence Co ions most likely plays the role in contributing to this extra chemical expansion.

Figure 4c, d shows the expansion curves of LP-73 and PrBCO samples at different atmospheres as a function of temperature. Comparing to the expansion curve of those materials in air, those of same starting components in the low $p\text{O}_2$ gas atmospheres seem to have lower inflection temperatures at which the chemical expansion begins to evolve. In general cases, samples with identical composition start to activate the oxygen vacancy formation at a certain driving force, i.e., the same oxygen chemical potential difference between the sample and the ambient gas phase. Since the LP-73 or PrBCO samples used in this study were prepared with same pretreatment process, the samples tested in a reduced gas phase reach the required minimum oxygen chemical potential difference to generate oxygen vacancy at a lower temperature. Meanwhile, the total expansion of the materials increases with the $p\text{O}_2$ decrease in the gas phase, because more oxygen vacancies can be created in the samples under low $p\text{O}_2$ environment, which leads to a greater chemical expansion [15, 41].

Electrical conductivity

Excellent IT-SOFC cathode materials require high ionic and electronic conductivity to reduce the ohmic impedance of the fuel cell. High electronic conductivity can ensure the rapid distribution of the electrons transferred from the anode through the external circuit at the cathode. In general, the electronic conductivity is much higher than the ionic conductivity in MIEC materials including $\text{LnBaCo}_2\text{O}_{5+\delta}$ so that the total conductivity obtained by the conventional DC four-electrode method can be considered as the electronic conductivity [42]. Figure 5a shows the electrical conductivity of $\text{La}_{1-x}\text{Pr}_x\text{BaCo}_2\text{O}_{5+\delta}$ cathode materials as a function of temperature at $p\text{O}_2 = 0.21$ atm.

It is obvious that the doping level of Pr has significant influence on the electrical conductivity of the LPBCO materials. The conductivity increases first and then decreases as Pr content increases. The highest conductivity values are all observed in LP-73 ($x = 0.3$). The same trends are found for the measured conductivities of these compositions in different $p\text{O}_2$ gas phases, as shown in Fig. S4.

Decrease in the conductivities of LPBCOs with reducing $p\text{O}_2$ shown in Fig. 5b and Fig. S5 suggests that LPBCOs under this study are generally p -type conductors [43]. That means the predominant charge carriers accounting for the electrical conductivity in LPBCOs are the electronic holes. The variation of the electronic holes numbers is associated with the oxygen vacancy concentration in MIECs. The iodometric titration of the as-calcined materials and the thermogravimetric analysis (Figure S3) reveal that the oxygen vacancy concentration in LPBCOs increases with Pr content under same temperatures. Especially, the abrupt oxygen vacancy concentration variation occurs between $x = 0.1$ and 0.5 . Such increased oxygen vacancy concentration can also be found with decreased Ln^{3+} ionic radius in LnBCO materials [38]. Increasing the oxygen vacancy concentration leads to a higher level reduction of Co^{4+} to Co^{3+} , which eventually lowers the charge carriers concentration and the Co–O covalent interaction as well in the materials [44]. For double-perovskite LPBCOs, introduction of small size Pr will increase the distortion of CoO_6 octahedron and therefore the O–Co–O angles [18]. It leads to the decreased overlap of Co:3d and O:2p orbitals and the energy band becomes broader, which increases the activation energy of polaron

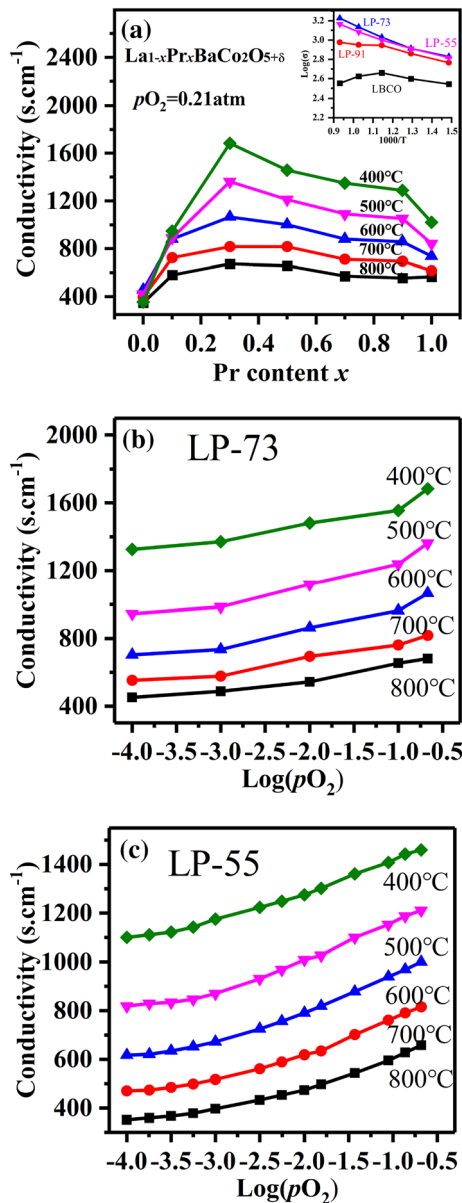


Figure 5 Variation of the electrical conductivity of a $\text{La}_{1-x}\text{Pr}_x\text{BaCo}_2\text{O}_{5+\delta}$ as a function of Pr content at $p\text{O}_2 = 0.21\text{atm}$, b LP-73, and c LP-55 as a function of $p\text{O}_2$ at different temperatures.

Table 1 The $\log(p\text{O}_2)$ dependency of the electrical conductivity of LP-73 and LP-55 in Fig. 5b, c

Samples	Temperature (°C)				
	400	500	600	700	800
LP-73	99.1	122.5	107.3	80.6	71.6
LP-55	112.5	125.2	119.8	107.7	91.8

transition and eventually results in the decreased electrical conductivity. In addition, doping with smaller Pr^{3+} causes the O^{2-} electron cloud to shift more toward it. This can increase the covalent effect of Pr–O bond and correspondingly reduce the distance between the O: 2d orbital center and the Fermi level, and finally reduces the conductivity of the sample. These effects explain the general conductivity variation tendency for those LPBCOs with higher Pr content which generally are in double-perovskite phases.

However, for LPBCOs with less Pr content ($x < 0.3$), the ceramics have disordered perovskite structure rather than the layered double perovskite. Because of the random distribution of Ln^{3+} and Ba^{2+} on A sites, the reduced A-site Ln^{3+} radius as Pr doping in LPBCO will normally lead to a shorter Co–O–Co bond length which increases the degree of the electron cloud overlap between Co ions and oxygen, and therefore facilitate the electron hopping between Co^{3+} and Co^{4+} [38]. In case of negligible Co^{4+} – Co^{3+} transition or oxygen vacancy concentration at a constant temperature, such effect will lead to an increased electrical conductivity, which is typically true for the LPBCO materials with $x < 0.3$. Although increasing Pr content still generates more oxygen vacancy in LPBCOs with $x < 0.3$, the concentration variation is relatively much lower and its consequent negative effects on the electrical conductivity are suppressed by the positive effect of reduced Co–O length. Obviously, the mentioned counterbalance effect is strongly dependent on the oxygen vacancy concentration level in the materials. With the further increase in oxygen vacancy levels in the lattice, the negative effect by the resulted relatively lower charge carrier concentration on the electrical conductivity becomes not trivial. The overall electrical conductivity enhancement effect by Pr doping in LPBCO at high temperatures becomes less significant.

The inset of Fig. 5a depicts the electrical conductivity variation of LPBCOs with different Pr doping vs. temperature. For the single-perovskite LPBCO materials, such as LaBCO and LP-91, a transition of *p*-type semiconductor to metal-like conduction behavior is observed. It is believed that the semiconducting behavior at low-temperature region can be ascribed to the enhanced charge carrier mobility induced by the thermal activation, whereas the decrease in the electrical conductivity at high temperature is mainly attributed to the reduction of the concentration of

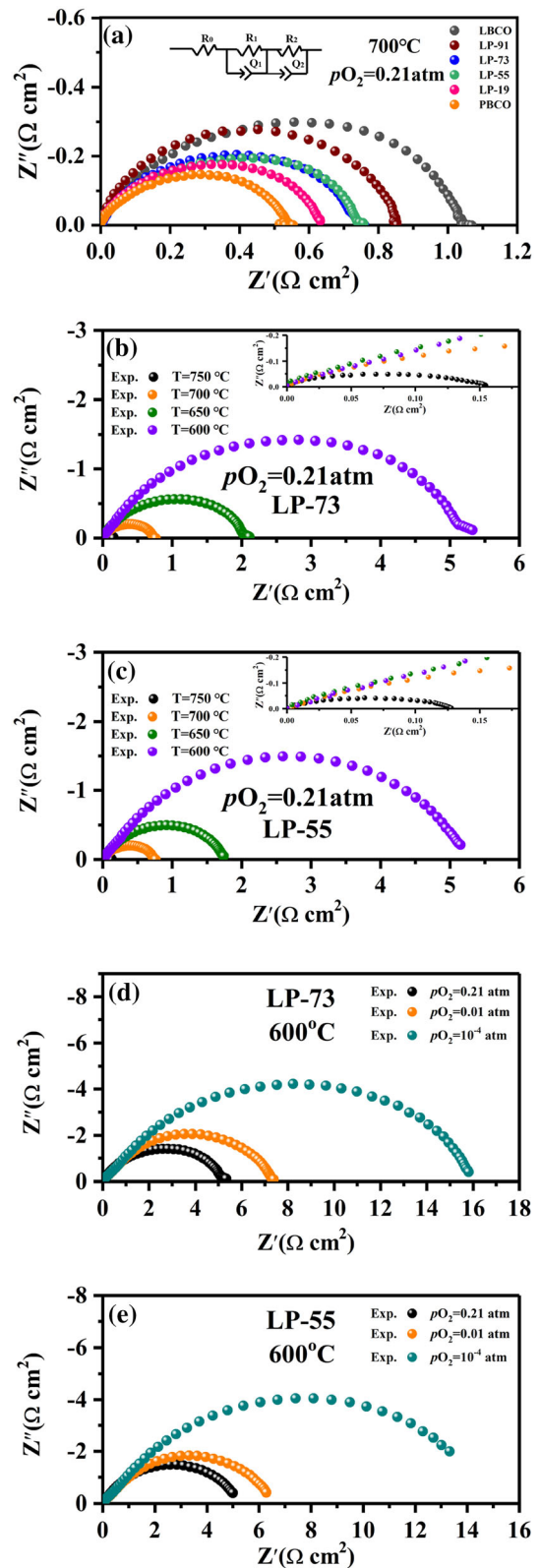
Figure 6 AC impedance spectra of **a** $\text{La}_{1-x}\text{Pr}_x\text{BaCo}_2\text{O}_{5+\delta}$ cathodes with various Pr doping (inset is the equivalent circuit model); **b** LP-73 and **c** LP-55 at different temperatures in air; **d** LP-73 and **e** LP-55 at 600 °C under different oxygen partial pressures.

charge carriers for *p*-type conducting MIECs. Especially for those LPBCO ceramics with higher Pr content ($x > 0.3$), the starting oxygen nonstoichiometry was already high enough that the charge carriers concentration becomes the main controlling factor accounting for the electrical conductivity variation. The oxygen loss induced by increasing temperature leads to the reduction of more Co^{4+} and therefore a further loss of charge carriers which continuously reduces the electrical conductivity.

Other than rising the temperature, reducing the $p\text{O}_2$ level also results in the formation of more oxygen vacancy concentration and therefore the decreased electrical conductivity whether the composition is either a single-perovskite phase (i.e., LP-73 in Fig. 5b) or a double-perovskite structure (i.e., LP-55 in Fig. 5c). The variation of the electrical conductivity vs $\log(p\text{O}_2)$ is roughly linear at a constant temperature for almost all the samples in this study (Fig. S5). The variation slopes of LP-73 and LP-55 are derived from the figures and listed in Table 1. The values fairly decrease with increasing the temperature. Interestingly, the $\log(p\text{O}_2)$ dependency of conductivity seems to become less at lower $p\text{O}_2$ range by carefully inspecting the data in Fig. 5b, c. The $\log(p\text{O}_2)$ dependency change with temperature and $p\text{O}_2$ levels could be ascribed to the variations of atomic structure and the charge carrier concentration as well. A further defect chemistry and thermodynamics investigation, especially the variation of oxygen nonstoichiometry with *T* and $p\text{O}_2$, would be necessary and helpful for the detailed and quantitative understanding of the relationship between the electrical conductivity and *T* and $p\text{O}_2$.

Electrochemical polarization

For MIEC materials, the oxygen exchange process on the cathode surface includes several sub-processes, such as oxygen diffusion, adsorption, dissociation, incorporation, and so on. When analyzed with electrochemical impedance, these sub-processes demonstrate different response time and response frequency



in EIS spectrum [45]. Figure 6a shows typical Nyquist plot of $\text{La}_{1-x}\text{Pr}_x\text{BaCo}_2\text{O}_{5+\delta}$ at 700 °C in air. Apparently, LPBCOs with different Pr contents exhibits large polarization difference. The polarization resistance generally decreases with the increase in Pr content. This is due to the higher oxygen vacancy concentrations in LPBCOs with higher Pr content. Similarly, the polarization resistance of a certain LPBCO material decreases with the increase in temperature (Fig. 6b) and with the decrease in the $p\text{O}_2$ (Fig. 6c) since the oxygen vacancy level increase as temperature increases and/or $p\text{O}_2$ decreases. In a word, more available oxygen vacancy defects in the lattice can generally enhance the oxygen surface exchange and the bulk diffusion and therefore reduce the cathodic polarization.

The area specific resistance (ASR) of each LPBCO under certain temperature and $p\text{O}_2$ was calculated by dividing the resistance span (the resistance difference between the high frequency and low frequency intersects of the Nyquist plot with the real coordinate) by the effective surface area of the symmetric cell. The ASR is compared with the several cathode materials which are in either single-perovskite or double-perovskite structures in Table S1. Clearly, the materials in this study have the comparative and even lower ASR values with some other double-perovskite materials. The corresponding Arrhenius diagram of the ASR of LPBCO materials measured in air is shown in Fig. 7. The activation energy values are estimated at 1.38, 1.48, 1.63, 1.60, 1.59, and 1.57 eV for LaBCO, LP-91, LP-73, LP-55, LP-19, and PrBCO, respectively.

As mentioned previously, the oxygen transport through the MIEC materials involves multiple electrochemical sub-processes among which one or few is the rate-determining step(s) (RDS) controlling the overall oxygen transport process. Analysis on the EIS

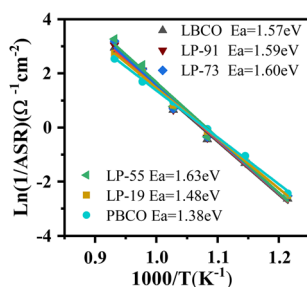


Figure 7 Arrhenius plots of the area specific resistance of $\text{La}_{1-x}\text{Pr}_x\text{BaCo}_2\text{O}_{5+\delta}$ ceramics.

spectrum can usually help rationalize and differentiate the process. As presented in Fig. 6c, the EIS spectrum typically consists of a depressed low-frequency (LF) semicircle and a high-frequency (HF) semicircle at low temperatures, which to some extent can conclude at least two sub-processes are involved in the whole oxygen transport process. As temperature increases, the HF semicircle merges into the LF semicircle. Conventional equivalent circuit modeling without process pre-identification usually leads to miss interpretation of the EIS spectra since different models may fit the data equally well. In this study, a distribution of relaxation times (DRT) technique [46–48] was further applied for identifying the main sub-processes involved in LPBCOs. The detailed methodology of DRT evaluation can be found elsewhere and a free MATLAB software called DRTtools was used to obtain the DRT spectra from the experimental EIS data [49]. This technique allows people to calculate the frequency-dependent DRT function $g(\tau)$ [which has the same unit as the polarization resistance and τ is the time constant corresponding to $(2\pi f)^{-1}$] from the discrete EIS data set. The $g(\tau)-\tau$ or $g(\tau)-f$ curve can be used to differentiate peaks for each substantial sub-process corresponding to its characteristic frequency. However, care should be taken in use of the DRT analysis. Due to the fact of discrete EIS data and the more-flattened $Z'-Z''$ spectrum of a depressed semicircle on the high and low frequency ends, discrepancy exists between the numerically derived DRT spectra and the theoretical DRT curve for ZARC models (i.e., R//CPE circuits) [49]. Minor pseudo-peaks not related to the ZARC models appeared in the numerically derived DRT spectra on the front and tail shoulders of the main peak [49]. This phenomenon also exists in the obtained DRT spectra from our EIS data of LPBCOs. The minor Pk1 and Pk3 peaks around the main Pk2 peak, as depicted in Fig. 8a and Fig. 8b, are no longer considered as actual responses of real electrochemical sub-processes. Only the LF and HF sub-processes corresponding to the Pk2 and Pk4 peaks in the DRT spectra are analyzed in the following discussion. The Pk2 or LF sub-process decreases its magnitude and shift to higher frequency as temperature rises, while the Pk2 or HF sub-process almost remains its magnitude only with the frequency shifting to the lower side. In terms of the peak intensity, Pk2 dominates the whole process at lower temperatures. The significantly reduced Pk2 peak makes it equivalently

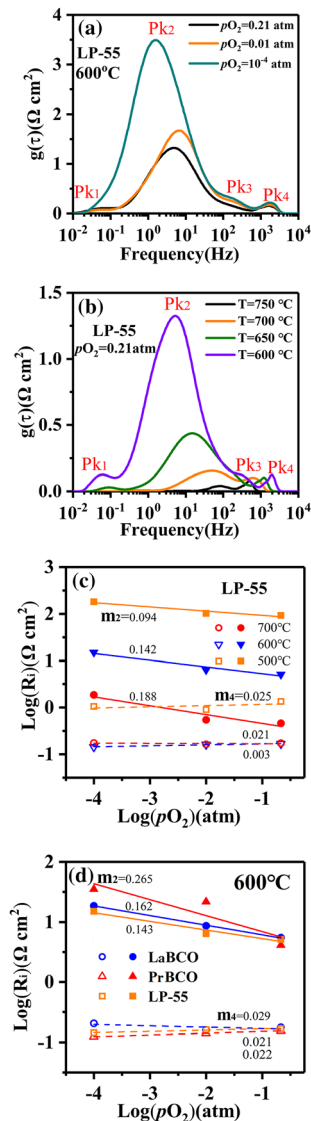


Figure 8 DRT analysis of the AC impedance of LP-55 **a** at different temperatures in air and **b** at different pO_2 at 600 °C; **c** polarization resistances of LP-55 versus pO_2 at different temperatures and **d** polarization resistances of different LPBCOs versus pO_2 at 600 °C.

important as Pk4 at $T \geq 700$ °C. The oxygen partial pressure also has important effects to these sub-processes, especially on Pk2 sub-process, as shown in Fig. 8a. It is obvious that Pk2 process becomes sharply increased in the whole oxygen transport process at sufficiently low pO_2 range, i.e., 10^{-4} atm. The unvaried Pk4's magnitude and peak frequency under various pO_2 indicate this sub-process is pO_2 independent.

An equivalent circuit with two R//CPE loops in series representing the Pk2 and Pk4 responses (as

shown in the inset of Fig. 6a) was adopted for most of the available EIS data analysis. In the equivalent circuit, L_0 and R_b represent the inductance of the measurement system and the ohmic resistance of the symmetric cell used in the EIS tests, and (R_1Q_1) and (R_2Q_2) represent the high- and low-frequency semi-circles, respectively. R_1 and R_2 are defined as the polarization resistance at high and low frequencies, respectively, and Q_1 and Q_2 are the HF and LF constant phase angle elements (CPE). The corresponding equivalent characteristic capacitance C_i of each constant phase angle element Q_i can be calculated by the following equations [28, 50]:

$$Z_Q = \frac{1}{Q(j\omega)^n} \quad (3)$$

$$C_i = \frac{(R_i Q_i)^{1/n_i}}{R_i} \quad (4)$$

where Z_Q is the impedance of a R//CPE circuit, ω is the angular frequency and n is an exponential term reflecting the homogeneity of the electrode system. Particularly, the constant phase element Q represents an ideal capacitor and an ideal resistor when $n = 1$ and $n = 0$, respectively. Table 2 lists the fitting parameters of the AC impedance spectra for the LP-55 electrode at different pO_2 at 600 °C.

In order to determine the nature of the dominating sub-process for the corresponding HF and LF impedances, the correlation between the electrode polarization resistance and the oxygen partial pressure is applied. Usually, the relationship can be expressed as [28, 50]:

$$R_i = k(pO_2)^{-m_i} \quad (5)$$

where k is a prefix constant, and m_i is an exponential parameter related to the rate-controlling step. R_i is the polarization resistance obtained by the equivalent circuit fitting in different atmospheres for the specific impedance arc. Figure 8d shows the relationship between the polarization impedance and oxygen partial pressure corresponding to the HF and LF responses at 500, 600, and 700 °C. It is found that the polarization resistance of HF process decreases with the increase in temperature and is insensitive to the change of oxygen partial pressure, i.e., the parameter m_1 in Eq. (5) for the HF polarization is about 0.02–0.03. It is therefore speculated that the high-frequency process is mostly dominated by the oxygen ions transfer through the

Table 2 Fitting parameters of AC impedance spectra for the LP-55 electrode at different oxygen partial pressures at 600 °C according to the equivalent circuit depicted in Fig. 6a

p_{O_2} atm	R_p ($\Omega \text{ cm}^2$)	HF (Pk4)				LF (Pk2)			
		R_1 ($\Omega \text{ cm}^2$)	Q_1 ($\Omega \text{ cm}^2 \text{ s}^{-n}$)	n_1	C_1 (F cm^{-2})	R_2 ($\Omega \text{ cm}^2$)	Q_2 ($\Omega \text{ cm}^2 \text{ s}^{-n}$)	n_2	C_2 (F cm^{-2})
0.21	5.31	0.17	4.16×10^{-3}	0.82	8.48×10^{-4}	5.14	2.02×10^{-2}	0.67	6.62×10^{-3}
10^{-2}	6.57	0.16	3.56×10^{-3}	0.85	9.33×10^{-4}	6.41	1.46×10^{-2}	0.65	4.09×10^{-3}
10^{-4}	15.18	0.14	3.07×10^{-3}	0.86	8.73×10^{-4}	15.04	1.45×10^{-2}	0.62	5.73×10^{-3}

electrode/electrolyte interface which is a p_{O_2} independent process [28]. On the other hand, the LF polarization resistance of LP-55 increases with the decrease in p_{O_2} , and the exponential parameter, m_2 , is generally estimated in a range of 0.1–0.2 at different temperatures. This value is very close to the characteristic p_{O_2} dependency of $\text{Log}(R_{\text{LF}})$ at 1/8 corresponding to the mono-electron charge transfer process $\text{O}_{\text{ad}}^{-1} + e^- = \text{O}_{\text{ad}}^{-2}$. Even the exceptional 1/4 dependency for PrBCO can also be ascribed to the two-electron charge transfer process $\text{O}_{\text{ad}} + 2e^- + \text{V}_{\text{O}}^{\bullet\bullet} = \text{O}_{\text{O}}^{\times}$ [50]. In other words, the LF impedance response of LP-55 is mainly dominated by the charge transfer process. Relatively, the DRT peak intensity of LF impedance is much larger than that of HF impedance, which indicates the charge transfer is the main rate-controlling step for the whole oxygen transfer process.

Conclusions

A series of A-site double-lanthanide-doped perovskites, $\text{La}_{1-x}\text{Pr}_x\text{BaCo}_2\text{O}_{5+\delta}$, were prepared to evaluate a materials design strategy for more efficient cathode materials. Particularly, the effect of Pr substitution for La on the structural, thermochemical, mechanical, electrical, and electrochemical properties of $\text{La}_{1-x}\text{Pr}_x\text{BaCo}_2\text{O}_{5+\delta}$ ($x = 0, 0.1, 0.3, 0.5, 0.7, 0.9, 1.0$) perovskite has been systematically investigated. $\text{La}_{1-x}\text{Pr}_x\text{BaCo}_2\text{O}_{5+\delta}$ exhibit a structural change from single perovskite (cubic Pm-3 m) to double perovskite (tetragonal, P4/mmm) upon increase in Pr doing level. Meanwhile, all the compositions demonstrate excellent chemical compatibility with $\text{Ce}_{0.8}\text{Gd}_{0.2}\text{O}_{1.9}$ (GDC) at 1000 °C in Air. The investigation found the La-Pr co-doping has significant effects on the electrical conductivity. The electrical

conductivity at 400–800 °C increased ($0 \leq x \leq 0.3$) firstly and then decreased ($0.3 \leq x \leq 1$) with the increase in Pr content. LP-73 ($x = 0.3$) in single-perovskite structure demonstrated the highest electrical conductivity in all the compositions under study while LP-55 ($x = 0.5$) presents the best among the double perovskites. Electrochemical impedance spectroscopy analysis shows that LBCOs have low area specific resistances (ASR). DRT spectra analysis along with the inspection of the Nyquist plot identified two sub-processes involved in the oxygen transport through the materials. Relatively, the low-frequency sub-process dominates the whole process and the charge transfer is believed as the rate-controlling step. The investigation generally concludes the double-lanthanide-doped LPBCO materials are a promising cathode for IT-SOFC and other electrochemical devices. But care should be taken regarding its thermal expansion. Although doping of Pr at A-site can reduce the thermal expansion of such double-perovskite materials, the overall chemical expansion coefficient is still high (over 20 ppm/K). Further improvements are still required.

Acknowledgements

The project was supported by the National Natural Science Foundation of China (Grant Nos. 52062002 and 51961006) and the Open Foundation of Guangxi Key Laboratory of Processing for Non-ferrous Metals and Featured Materials, Guangxi University, China (2021GXYSOF01).

Supplementary Information: The online version contains supplementary material available at <http://doi.org/10.1007/s10853-022-07497-x>.

References

- [1] Mahato N, Banerjee A, Gupta A, Omar S, Balani K (2015) Progress in material selection for solid oxide fuel cell technology: a review. *Prog Mater Sci* 72:141–337. <https://doi.org/10.1016/j.pmatsci.2015.01.001>
- [2] Steel BCH, Heinzel A (2001) Materials for fuel-cell technologies. *Nature* 414:345–352. <https://doi.org/10.1038/35104620>
- [3] Gomez AEM, Lamas DG, Leyva AG, Sacanell J (2019) Nanostructured $\text{La}_{0.5}\text{Ba}_{0.5}\text{CoO}_3$ as cathode for solid oxide fuel cells. *Ceram Int* 45:14182–14187. <https://doi.org/10.1016/j.ceramint.2019.04.122>
- [4] Staffell I, Scamman D, Abad AV, Balcombe P, Dodds PE, Ekins P, Shah N, Ward KR (2019) The role of hydrogen and fuel cells in the global energy system. *Energy Environ Sci* 12:463–491. <https://doi.org/10.1039/c8ee01157e>
- [5] Abdalla AM, Hossain S, Azad AT, Petra PMI, Begum F, Eriksson SG, Azad AK (2018) Nanomaterials for solid oxide fuel cells: a review. *Renew Sustain Energy Rev* 82:353–368. <https://doi.org/10.1016/j.rser.2017.09.046>
- [6] Park B-K, Cox D, Barnett SA (2021) Effect of nanoscale $\text{Ce}_{(0.8)}\text{Gd}_{(0.2)}\text{O}_{(2-\delta)}$ infiltrant and steam content on $\text{Ni}-(\text{Y}_2\text{O}_3)_{(0.08)}(\text{ZrO}_2)_{(0.92)}$ fuel electrode degradation during high-temperature electrolysis. *Nano Lett* 21:8363–8369. <https://doi.org/10.1021/acs.nanolett.1c02937>
- [7] Rupp GM, Glowacki M, Fleig J (2016) Electronic and ionic conductivity of $\text{La}_{0.95}\text{Sr}_{0.05}\text{Ga}_{0.95}\text{Mg}_{0.05}\text{O}_{3-\delta}$ (LSGM) single crystals. *J Electrochem Soc* 163:F1189–F1197. <https://doi.org/10.1149/2.0591610jes>
- [8] Liu M, Gao J, Liu X, Meng G (2011) High performance of anode supported $\text{BaZr}_{0.1}\text{Ce}_{0.7}\text{Y}_{0.2}\text{O}_{3-\delta}$ (BZCY) electrolyte cell for IT-SOFC. *Int J Hydrogen Energy* 36:13741–13745. <https://doi.org/10.1016/j.ijhydene.2011.07.087>
- [9] Kim J-H, Manthiram A (2015) Layered $\text{LnBaCo}_2\text{O}_{5+\delta}$ perovskite cathodes for solid oxide fuel cells: an overview and perspective. *J Mater Chem A* 3:24195–24210. <https://doi.org/10.1039/c5ta06212h>
- [10] Aziz A-J, Baharuddin NA, Somalu MR, Muchtar A (2020) Review of composite cathodes for intermediate-temperature solid oxide fuel cell applications. *Ceram Int* 46:23314–23325. <https://doi.org/10.1016/j.ceramint.2020.06.176>
- [11] Lyu YM, Xie JT, Wang DB, Wang R (2020) Review of cell performance in solid oxide fuel cells. *J Mater Sci* 55:7184–7207. <https://doi.org/10.1007/s10853-020-04497-7>
- [12] Shao Z, Haile SM (2004) A high-performance cathode for the next generation of solid-oxide fuel cells. *Nature* 431:170–173. <https://doi.org/10.1038/nature02863>
- [13] Kim J-H, Prado F, Manthiram A (2008) Characterization of $\text{GdBa}_{1-x}\text{Sr}_x\text{Co}_2\text{O}_{5+\delta}$ double perovskites as cathodes for solid oxide fuel cells. *J Electrochem Soc* 155:B1023–B1028. <https://doi.org/10.1149/1.2965792>
- [14] Zhou QJ, Wang F, Shen Y, He TM (2010) Performances of $\text{LnBaCo}_2\text{O}_{5+x}-\text{Ce}_{0.8}\text{Sm}_{0.2}\text{O}_{1.9}$ composite cathodes for intermediate-temperature solid oxide fuel cells. *J Power Sources* 195:2174–2181. <https://doi.org/10.1016/j.jpowsour.2009.10.062>
- [15] Zhao L, Shen F, He BB, Chen F, Xia CR (2011) Synthesis, characterization and evaluation of $\text{PrBaCo}_{2-x}\text{Fe}_x\text{O}_{5+\delta}$ as cathodes for intermediate-temperature solid oxide fuel cells. *Int J Hydrog Energy* 36:3658–3665. <https://doi.org/10.1016/j.ijhydene.2010.12.064>
- [16] Petrov AN, Kononchuk OF, Andreev AV, Cherepanov P (1995) Crystal structure, electrical and magnetic properties of $\text{La}_{1-x}\text{Sr}_x\text{CoO}_{3-y}$. *Solid State Ionics* 80:189–199. [https://doi.org/10.1016/0167-2738\(95\)00114-L](https://doi.org/10.1016/0167-2738(95)00114-L)
- [17] Mitberg EB, Patrakee MV, Leonidov IA, Kozhevnikov VL, Poeppelmeier KR (2000) High-temperature electrical conductivity and thermopower in nonstoichiometric $\text{La}_{1-x}\text{Sr}_x\text{CoO}_{3-\delta}$ ($x=0.6$). *Solid State Ionics* 130:325–330. [https://doi.org/10.1016/S0167-2738\(00\)00670-6](https://doi.org/10.1016/S0167-2738(00)00670-6)
- [18] Tai LW, Nasrallah MN, Anderson HU, Sparlin DM, Sehlin SR (1995) Structure and electrical-properties of $\text{La}_{1-x}\text{Sr}_x\text{Co}_{1-y}\text{Fe}_y\text{O}_3$. 2. The system $\text{La}_{1-x}\text{Sr}_x\text{Co}_{0.2}\text{Fe}_{0.8}\text{O}_3$. *Solid State Ionics* 76:273–283. [https://doi.org/10.1016/0167-2738\(94\)00244-m](https://doi.org/10.1016/0167-2738(94)00244-m)
- [19] Huang YW, Ding JW, Xia YP, Miao LN, Li K, Zhang QP, Liu W (2020) $\text{Ba}_{0.5}\text{Sr}_{0.5}\text{Co}_{0.8-x}\text{Fe}_{0.2}\text{Nb}_x\text{O}_{3-\delta}$ ($x \leq 0.1$) as cathode materials for intermediate temperature solid oxide fuel cells with an electron-blocking interlayer. *Ceram Int* 46:10215–10223. <https://doi.org/10.1016/j.ceramint.2020.01.013>
- [20] Bao SY, Ma CR, Chen G, Xu X, Enriquez E, Chen CL, Zhang YM, Bettisjr JL, Whangbo WH, Dong C, Zhang QY (2014) Ultrafast atomic layer-by-layer oxygen vacancy-exchange diffusion in Double-Perovskite $\text{LnBaCo}_2\text{O}_{5.5+\delta}$ thin films. *Sci Rep* 4:4726. <https://doi.org/10.1038/srep04726>
- [21] Chen T, Zhao H, Xie Z, Xu N, Lu Y (2015) Oxygen permeability of $\text{Ce}_{0.8}\text{Sm}_{0.2}\text{O}_{2-\delta}-\text{LnBaCo}_2\text{O}_{5+\delta}$ ($\text{Ln}=\text{La}, \text{Nd}, \text{Sm}, \text{and Y}$) dual-phase ceramic membranes. *Ionics* 21:1683–1692. <https://doi.org/10.1007/s11581-014-1327-5>
- [22] Zhang LK, Li SL, Xia T, Sun LP, Hou LH, Zhao H (2018) Co-deficient $\text{PrBaCo}_{2-x}\text{O}_{6-\delta}$ perovskites as cathode materials for intermediate-temperature solid oxide fuel cells: Enhanced electrochemical performance and oxygen reduction kinetics. *Int J Hydrog Energy* 43:3761–3775. <https://doi.org/10.1016/j.ijhydene.2018.01.018>

- [23] Taskin AA, Lavrov AN, Ando Y (2005) Achieving fast oxygen diffusion in perovskites by cation ordering. *Appl Phys Lett* 86:091910. <https://doi.org/10.1063/1.1864244>
- [24] Adachi S, Wakana H, Tanabe K (2007) Fabrication of ramp-edge Josephson junctions using LnBCO superconductors (Ln = Yb, Y and Sm). *Physica C* 460:1365–1366. <https://doi.org/10.1016/j.physc.2007.04.039>
- [25] Bernuy-Lopez C, Hydalsvik K, Einarsrud MA, Grande T (2016) Effect of A-site cation ordering on chemical stability, oxygen stoichiometry and electrical conductivity in layered $\text{LaBaCo}_2\text{O}_{5+\delta}$ double Perovskite. *Materials* 9:154. <https://doi.org/10.3390/ma9030154>
- [26] Bernuy-Lopez C, Rioja-Monllor L, Nakamura T, Ricote S, O'Hayre R, Amezawa K, Einarsrud M-A, Grande T (2018) Effect of cation ordering on the performance and chemical stability of layered double Perovskite cathodes. *Materials* 11:196. <https://doi.org/10.3390/ma11020196>
- [27] Zhang K, Ge L, Ran R, Shao Z, Liu S (2008) Synthesis, characterization and evaluation of cation-ordered $\text{LnBaCo}_2\text{O}_{5+\delta}$ as materials of oxygen permeation membranes and cathodes of SOFCs. *Acta Mater* 56:4876–4889. <https://doi.org/10.1016/j.actamat.2008.06.004>
- [28] Chen DJ, Ran R, Zhang K, Wang J, Shao ZP (2009) Intermediate-temperature electrochemical performance of a polycrystalline $\text{PrBaCo}_2\text{O}_{5+\delta}$ cathode on samarium-doped ceria electrolyte. *J Power Sources* 188:96–105. <https://doi.org/10.1016/j.jpowsour.2008.11.045>
- [29] Wang ZH, Liu YH, Chen YQ, Yang L, Wang Y, Wei MR (2019) A-site cation-ordered double perovskite $\text{PrBaCo}_2\text{O}_{5+\delta}$ oxide as an anion-inserted pseudocapacitor electrode with outstanding stability. *J Alloys Compd* 810:151830. <https://doi.org/10.1016/j.jallcom.2019.151830>
- [30] Ding H, Xue X (2010) $\text{PrBa}_{0.5}\text{Sr}_{0.5}\text{Co}_2\text{O}_{5+\delta}$ layered perovskite cathode for intermediate temperature solid oxide fuel cells. *Electrochim Acta* 55:3812–3816. <https://doi.org/10.1016/j.electacta.2010.01.104>
- [31] Chen Y, Yoo S, Choi Y, Kim JH, Ding Y, Pei K, Murphy R, Zhang Y, Zhao B, Zhang W, Chen H, Chen Y, Yuan W, Yang C, Liu M (2018) A highly active, CO_2 -tolerant electrode for the oxygen reduction reaction. *Energy Environ Sci* 11:2458–2466. <https://doi.org/10.1039/C8EE01140K>
- [32] Wei B, Schroeder M, Martin M (2018) Surface cation segregation and chromium deposition on the double-Perovskite Oxide $\text{PrBaCo}_2\text{O}_{5+\delta}$. *Acs Appl Mater Int* 10:8621–8629. <https://doi.org/10.1021/acsami.7b17881>
- [33] Vollestad E, Schrade M, Segalini J, Strandbakke R, Norby T (2017) Relating defect chemistry and electronic transport in the double perovskite $\text{Ba}_{1-x}\text{Gd}_{0.8}\text{La}_{0.2+x}\text{Co}_2\text{O}_{6-\delta}$ (BGLC). *J Mater Chem A* 5:15743–15751. <https://doi.org/10.1039/c7ta02659e>
- [34] Saccoccio M, Jiang CL, Gao Y, Chen DJ, Ciucci F (2017) Nb-substituted $\text{PrBaCo}_2\text{O}_{5+\delta}$ as a cathode for solid oxide fuel cells: a systematic study of structural, electrical, and electrochemical properties. *Int J Hydrog Energy* 42:19204–19215. <https://doi.org/10.1016/j.ijhydene.2017.06.056>
- [35] Mehranjani AS, Cumming DJ, Sinclair DC, Rothman RH (2017) Low-temperature co-sintering for fabrication of zirconia/ceria bi-layer electrolyte via tape casting using a Fe_2O_3 sintering aid. *J Eur Ceram Soc* 37:3981–3993. <https://doi.org/10.1016/j.jeurceramsoc.2017.05.018>
- [36] Frontera C, Rodriguez-Carvajal J (2004) FULLPROF as a new tool for flipping ratio analysis: further improvements. *Physica B* 350:E731–E733. <https://doi.org/10.1016/j.physb.2004.03.192>
- [37] Shannon RD (1976) Revised effective ionic radii and systematic studies of interatomic distances in halides and chalcogenides. *Acta Crystallogr Se A* 32:751–767. <https://doi.org/10.1107/S0567739476001551>
- [38] Kim J-H, Manthiram A (2008) $\text{LnBaCo}_2\text{O}_{5+\delta}$ oxides as cathodes for intermediate-temperature solid oxide fuel cells. *J Electrochem Soc* 155:B385–B390. <https://doi.org/10.1149/1.2839028>
- [39] Yadav M, Gong WQ, Jacobson AJ (2011) Electrically driven oxygen separation through gadolinia-doped ceria using $\text{PrBaCo}_2\text{O}_{5+x}$ and $\text{NdBaCo}_2\text{O}_{5+x}$ electrodes. *J Solid State Electrochem* 15:293–301. <https://doi.org/10.1007/s10008-010-1082-0>
- [40] Jin FJ, Xu HW, Long W, Shen Y, He TM (2013) Characterization and evaluation of double perovskites $\text{LnBaCoFeO}_{5+\delta}$ (Ln = Pr and Nd) as intermediate-temperature solid oxide fuel cell cathodes. *J Power Sources* 243:10–18. <https://doi.org/10.1016/j.jpowsour.2013.05.187>
- [41] Chatterjee A, Caicedo JM, Ballesteros B, Santiso J (2018) An in operando study of chemical expansion and oxygen surface exchange rates in epitaxial $\text{GdBaCo}_2\text{O}_{5.5}$ electrodes in a solid-state electrochemical cell by time-resolved X-ray diffraction. *J Mater Chem A* 6:12430–12439. <https://doi.org/10.1039/c8ta02790k>
- [42] Liu YH, Pan ZF, Zhao XF, Zhong SH, Chen XY, Wang C (2021) Performance of $\text{PrBaCo}_2\text{O}_{5+\delta}$ impregnated $\text{La}_{0.6}\text{Sr}_{0.4}\text{Co}_{0.2}\text{Fe}_{0.8}\text{O}_{3-\delta}$ composites as potential cathode materials for solid oxide fuel cells. *J Alloys Compd* 886:161155. <https://doi.org/10.1016/j.jallcom.2021.161155>
- [43] Lee D, Kim D, Son SJ, Kwon Y, Lee Y, Ahn J-H, Joo JH (2019) Simultaneous A- and B- site substituted double perovskite ($\text{AA}'\text{B}_2\text{O}_{5+\delta}$) as a new high-performance and redox-stable anode material for solid oxide fuel cells. *J Power Sources* 434:226743. <https://doi.org/10.1016/j.jpowsour.2019.226743>

- [44] Jiang L, Li FS, Wei T, Zeng R, Huang YH (2014) Evaluation of $\text{Pr}_{1-x}\text{Ba}_x\text{Co}_2\text{O}_{5+\delta}$ ($x=0-0.30$) as cathode materials for solid-oxide fuel cells. *Electrochim Acta* 133:364–372. <https://doi.org/10.1016/j.electacta.2014.04.064>
- [45] Sun CZ, Kong Y, Shao L, Zhang Q, Wu X, Zhang NQ, Sun KN (2019) Significant zirconium substitution effect on the oxygen reduction activity of the cathode material $\text{NdBaCo}_2\text{O}_{5+\delta}$ for solid oxide fuel cells. *ACS Sustain Chem Eng* 7:11603–11611. <https://doi.org/10.1021/acssuscchemeng.9b01486>
- [46] Sonn V, Leonide A, Ivers-Tiffée E (2008) Combined deconvolution and CNLS fitting approach applied on the impedance response of technical Ni/8YSZ cermet electrodes. *J Electrochem Soc* 155:B675–B679. <https://doi.org/10.1149/1.2908860>
- [47] Hayd J, Ivers-Tiffée E (2013) Detailed electrochemical study on nanoscaled $\text{La}_{0.6}\text{Sr}_{0.4}\text{CoO}_{3-\delta}$ SOFC thin-film cathodes in dry, humid and CO_2 -containing atmospheres. *J Electrochem Soc* 160:F1197–F1206. <https://doi.org/10.1149/2.026311jes>
- [48] Zhang YX, Chen Y, Yan MF, Chen FL (2015) Reconstruction of relaxation time distribution from linear electrochemical impedance spectroscopy. *J Power Sources* 283:464–477. <https://doi.org/10.1016/j.jpowsour.2015.02.107>
- [49] Wan TH, Saccoccio M, Chen C, Ciucci F (2015) Influence of the discretization methods on the distribution of relaxation times deconvolution: implementing radial basis functions with DRTtools. *Electrochim Acta* 184:483–499. <https://doi.org/10.1016/j.electacta.2015.09.097>
- [50] Escudero MJ, Aguadero A, Alonso JA, Daza L (2007) A kinetic study of oxygen reduction reaction on La_2NiO_4 cathodes by means of impedance spectroscopy. *J Electroanal Chem* 611:107–116. <https://doi.org/10.1016/j.jelechem.2007.08.006>

Publisher's Note Springer Nature remains neutral with regard to jurisdictional claims in published maps and institutional affiliations.